Heterogeneous degradation of organic contaminants in the photo-Fenton reaction employing pure cubic β-Fe$_2$O$_3$

Yuanming Zhang[a], Ningsi Zhang[a], Tiantian Wang[c], Huiting Huang[a], Yong Chen[a], Zhaosheng Li[a,b,*], Zhigang Zou[a,b]

[a] Collaborative Innovation Center of Advanced Microstructures, National Laboratory of Solid State Microstructures, College of Engineering and Applied Science, Nanjing University, 22 Hankou Road, Nanjing, 210093, People's Republic of China
[b] Jiangsu Key Laboratory for Nano Technology, Nanjing University, 22 Hankou Road, Nanjing, 210093, People's Republic of China
[c] State Key Laboratory of Pharmaceutical Biotechnology, Nanjing University, Nanjing, 210093, People's Republic of China
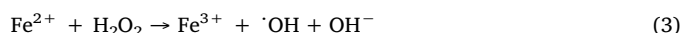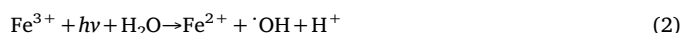
ABSTRACT

Pure cubic β-Fe$_2$O$_3$ crystal, which can absorb visible light (< 650 nm) on account of the bandgap of 1.9 eV as a direct bandgap semiconductor, was employed as a low-cost and non-toxic catalyst for photo-Fenton reaction in this article. Diverse organic contaminants including rhodamine B (RhB), methyl orange (MO), alizarin red (AR) and phenol can be effectively degraded. In particular, the degradation of RhB were investigated detailedly. As such, hydroxyl radicals (˙OH) were verified to act as considerable active species for the process by using terephthalic acid as an indicator. Degradation mechanism and intermediates of phenol in the photo-Fenton reaction was discovered by virtue of liquid chromatography-mass spectrometry (LC−MS). Notably, hydroxylation of phenol generated some intermediates, which are converted into H$_2$O and CO$_2$ eventually.

1. Introduction

Industrial wastewater treatment has been concerned for a long time, since it seriously endangers human health [1–5]. Advanced oxidation processes (AOPs) (O$_3$/ultraviolet, O$_3$/H$_2$O$_2$, ultraviolet/H$_2$O$_2$, ultraviolet/H$_2$O$_2$/catalyst, H$_2$O$_2$/Fe^{2+}) with high selectivity and environmental friendliness were used to oxidize various classes of organic contaminants, owing to the production of transitory species (˙OH). Fenton reaction, as one of the AOPs, was playing an indispensable role in the treatment of highly recalcitrant compounds by the ˙OH radicals, which were generated from the decomposition of H$_2$O$_2$ [6–14]. In case of photo-Fenton reaction, iron cycling between ΞFe^{2+} and ΞFe^{3+} occurred under light irradiation, and H$_2$O$_2$ was more easily converted to ˙OH compared to Fenton reaction. The photo-Fenton reaction can overcome the shortcoming of slow dynamics of the conventional Fenton process, therefore it is an attractive candidate for exhaustive removal of different stubborn contaminants [15,16]. Hydroxyl radicals were identified by reactions (1), (2) and (3), which can mineralize target organic contaminants [17,18].

$$H_2O_2 + h\nu \rightarrow {}^{\cdot}OH + {}^{\cdot}OH \tag{1}$$

$$Fe^{3+} + h\nu + H_2O \rightarrow Fe^{2+} + {}^{\cdot}OH + H^+ \tag{2}$$

$$Fe^{2+} + H_2O_2 \rightarrow Fe^{3+} + {}^{\cdot}OH + OH^- \tag{3}$$

The mitigation routes employed in the current large-scale pollution requirements were both cost-effective and significant. Iron-based semiconductor materials for photo-Fenton reaction provided a blameless pathway for future environmental governance [19–25].

The iron-based semiconductors included mainly oxides [26–31], sulfides [32–34], carbide [35], and composite materials [36–38], such as Fe$_2$O$_3$, Fe$_3$O$_4$, FeS, Fe$_3$C, α-Fe$_2$O$_3$/graphene oxide and so on. Distinct strategies such as copious heterojunction structure [39,40], nano regulation [41,42] and multifarious doping [43–45] had been implemented to improve the catalytic properties of these materials. For instance, Zhang and co-workers [46] reported the TiO$_2$/Fe$_2$TiO$_5$/Fe$_2$O$_3$ triple-heterojunction exhibited better catalytic activity of degrade MO and phenol than Fe$_2$O$_3$. Similarly, Wang et al [47] fabricated SnO$_2$-encapsulated α-Fe$_2$O$_3$ (Fe$_2$O$_3$@SnO$_2$) nanocubes to degrade RhB. Ma and co-workers [48] took γ-Fe$_2$O$_3$/ZnFe$_2$O$_4$ as an effective catalyst for the degradation and mineralization of Orange II with H$_2$O$_2$ under visible light irradiation.

In the aforementioned works, Fe$_2$O$_3$ was a widely studied catalytic

material due to the low cost, abundant reserves and suitable bandgap [49,50]. However, to the best of our knowledge, α-Fe$_2$O$_3$ and γ-Fe$_2$O$_3$ phases have been intensively studied. The application of cubic β-Fe$_2$O$_3$ in photo-Fenton reaction has not been well studied, though it can absorb visible light with wavelength smaller than 650 nm. In this study, it is found that the β-Fe$_2$O$_3$/H$_2$O$_2$/light system can effectively degrade various dyes and phenol. The apparent kinetic rate was 2.027×10^{-2} min^{-1} following pseudo first order kinetics for the degradation of RhB. With the help of LC−MS, we detected main intermediates in the process of phenol degradation and gave the analysis of degradation mechanism.

2. Experimental

2.1. Synthesis of pure cubic β-Fe$_2$O$_3$

In the typical reaction procedure, Fe$_2$(SO$_4$)$_3$ (15 mmol) and Na$_2$SO$_4$ (15 mmol) were respectively dissolved in 15 ml of deionized water, which were totally dissolved, continuous stirred for 12 h and evaporated at 70 °C in an oven. Thereupon, light yellow FeNa(SO$_4$)$_2$ powder was obtained. FeNa(SO$_4$)$_2$ and NaCl were ball milled in a molar ratio of 1–4 in the glove box, in order to prevent the effect of moisture in the air. Subsequently, the milled powder was calcined at 450 °C for 1 h in the muffle furnace. Finally, pure cubic β-Fe$_2$O$_3$ can be obtained after the incompletely reacted FeNa(SO$_4$)$_2$ and NaCl powders were wasted by deionized water.

When the milled FeNa(SO$_4$)$_2$ and NaCl powder was calcined at 600 °C for 1 h, pure α-Fe$_2$O$_3$ was obtained. Mixed phases of β-Fe$_2$O$_3$ and α-Fe$_2$O$_3$ were obtained, when the calcined temperature is within 450–600 °C.

2.2. Measurement of photo-Fenton reaction

The photo-Fenton measurement of the as-prepared samples was carried out in a photoreactor by degradation of RhB, MO, AR and phenol under visible-light irradiation. β-Fe$_2$O$_3$ catalyst (30 mg), aqueous solution of dye (100 mL, 20 mg/L) and H$_2$O$_2$ (0.04 M, 0.22 M, 0.4 M) were stirred for 40 min to achieve an adsorption-desorption equilibrium. A 300 W Xenon lamp served as the light source ($\lambda > 420$ nm), and the solution initial pH was about 4, then the solution (3 ml) was took out with a syringe equipped with a filter head intervals 20 min during the reactivity. Degradation efficiency (%) is equal to $[(C_0 - C)/C_0] \times 100\%$, where C_0 was the initial dye concentration (the experimental device was showed in Fig. S1 for dye and phenol degradation by photo-Fenton reaction). Cooling circulating water can effectively keep the system temperature stable. In order to explore the stability and reusability of catalysts, the above experiment was repeated for three times for the RhB degradation. The mass of the catalysts was 30, 25 and 21 mg, respectively. Using 60 mg catalyst, the degradation of phenol (3 mg/L) was carried out without modulating pH of solution, and the extracted solution was added to 120 μL of tertiary butanol in order to inhibit the residual ·OH from affecting the experimental results.

The concentration of phenol was measured by the 4-aminoantipyrine method, which was used to evaluate the effect of β-Fe$_2$O$_3$/H$_2$O$_2$/ light system initially. The phenol conversion was detected by LC–MS (Waters SQD2) equipped with an Agilent DB-17MS column (30 mm × 0.25 μm × 0.25 mm) for the sake of more accurate results in the process of phenol degradation. The mobile phase was water and methanol mixed in a volume ratio of 60 to 35, which was at a flow rate of 0.6 mL/min.

2.3. Characterization

The crystal phases of the samples were investigated on a Rigaku Ultima III X-ray diffractometer (Japan, Cu Kα radiation, 40 kV and 40 mA). The surface morphology of the as-prepared samples was identified by the scanning electron microscope (SEM, Japan, HITACHI S3400 N II). An automatic surface area analyzer (USA, Micromeritics ASAP 2020) was applied to measure the specific surface area of the as-prepared samples from the adsorption branch of N$_2$ isotherm. The pore size distribution was calculated from Barrett-Joyner-Halenda method for mesopores. Fourier transform infrared spectra (FT-IR) of the samples were obtained from the NEXUS870 by scanning from 4000 to 400 cm^{-1} in a KBr tablets. Photoluminescence (PL) spectra were employed on a fluorescence spectrometer (USA, VARIAN CARY Eclipse) fixed at 285 nm of excitation wavelength with 5 nm excitation slit width and 10 nm emission slit width at room temperature. Time-resolved photoluminescence (TR-PL) decay spectra were detected by a Fluorescence-3 spectrometer (Horiba Scientific) with an excitation wavelength of 385 nm (fluorescent peak). The X-ray photoelectric spectra (XPS) (Japan, ULVAC-PHI, PHI 5000 Versa Probe) were used to determine the surface chemical state. The optical properties were studied by UV–vis spectrophotometer (Japan, Shimadzu, UV-2550) fitted with a reference BaSO$_4$. The mineralization rate of RhB solution was detected with a TOC analyzer (Japan, Shimadzu, TOC-L). The total iron content of the solution was detected the atomic absorption spectrometer (AAS, 180-80, Hitachi, Japan).
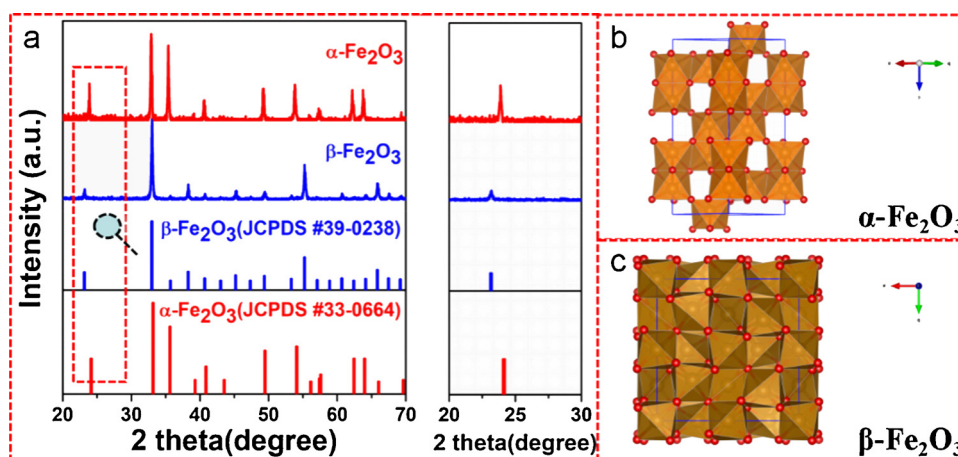

Fig. 1. a) XRD patterns of β-Fe$_2$O$_3$ (blue) and commercial α-Fe$_2$O$_3$ (red), crystallographic images of α-Fe$_2$O$_3$ (b) and β-Fe$_2$O$_3$ (c) (For interpretation of the references to colour in this figure legend, the reader is referred to the web version of this article).
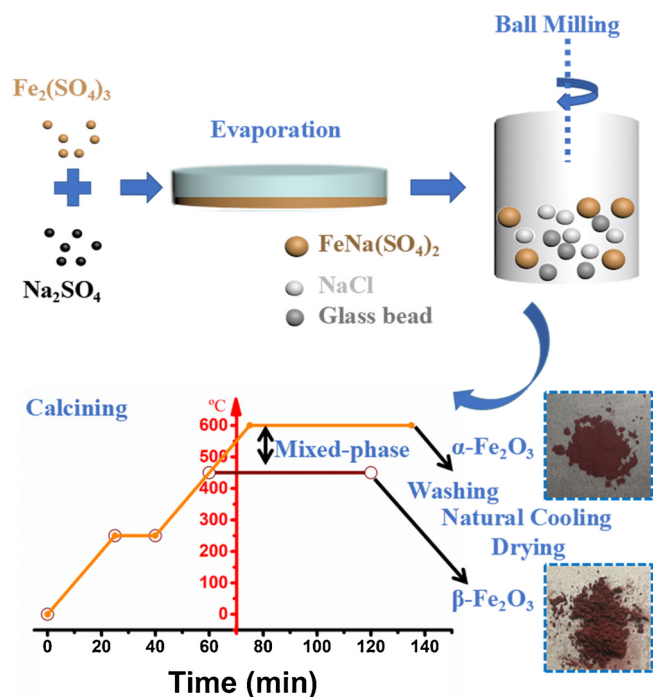
Fig. 2. Schematic illustration of the synthesis process of α-Fe$_2$O$_3$, mixed-phase and β-Fe$_2$O$_3$.

3. Results and discussion

3.1. Characterizations of β-Fe$_2$O$_3$

As illustrated in the Fig. 1a, the strong diffraction peaks at 23.2°,

33.0°, 35.7°, 38.3°, 40.7°, 45.2°, 49.4°, 55.2° and 65.9° can be indexed to the (211), (222), (321), (400), (411), (332), (431), (440) and (622) planes of standard pattern of cubic β-Fe$_2$O$_3$ phase (JCPDS #39-0238), respectively, and no additional impurity diffraction peaks were detected. In the enlarged XRD pattern around 2θ = 20-30°, the strong diffraction peak at 23.2° can be indexed to the (211) of β-Fe$_2$O$_3$, but the strong diffraction peaks at 24.1° can be indexed to the (012) of α-Fe$_2$O$_3$. Moreover, β-Fe$_2$O$_3$ and α-Fe$_2$O$_3$ held a bixbyite structure (*Ia3*) and (*R3c*), respectively. XPS measurements were further conducted to investigate the chemical compositions (Fig. S2). As shown in Fig. S2b, the spectrum for C 1 s was fitted at 284 and 288 eV, representing hydrocarbon (C−C), alcohol (C=O) and the other bond type, respectively. The peaks at 710.5 eV and 724.1 eV were all attributed to the Fe^{3+} (Fig. S2c), which can be assigned to Fe 2p$_{3/2}$ and Fe 2p$_{1/2}$. Fig. S2c showed that O 1 s spectrum can be divided into three different peaks around 529.9, 531.3 and 532.5 eV, which are mainly attributed to the characteristic binding energies of Fe-O, O component in oxygen vacancy, and the chemisorbed O, respectively.

The strategy for synthesizing β-Fe$_2$O$_3$ was schematically depicted in Fig. 2. The FeNa(SO$_4$)$_2$ of low temperature evaporation should be kept dry. In this ball milling process, it was vital to avoid the effects of moisture in the surrounding environment. In the subsequent calcining process, pure β-Fe$_2$O$_3$ appeared when the calcined temperature was 450 °C, which was completely converted into pure α-Fe$_2$O$_3$ when the calcined temperature was 450 °C. However, the mixed-phase of the two was obtained when the calcined temperature was with 450–600 °C (Fig. S4).

As shown in Fig. 3a, a small number of particles aggregated to form clusters on the surfaces of the samples. According to previous report [51], it was feasible to increase the β-Fe$_2$O$_3$ purity by adding molten salt, which had the same structure. The particles were with side lengths of approximately 0.2-0.4 μm as shown in Fig. 3b. The specific surface area and pore size distributions of the β-Fe$_2$O$_3$ particles were measured
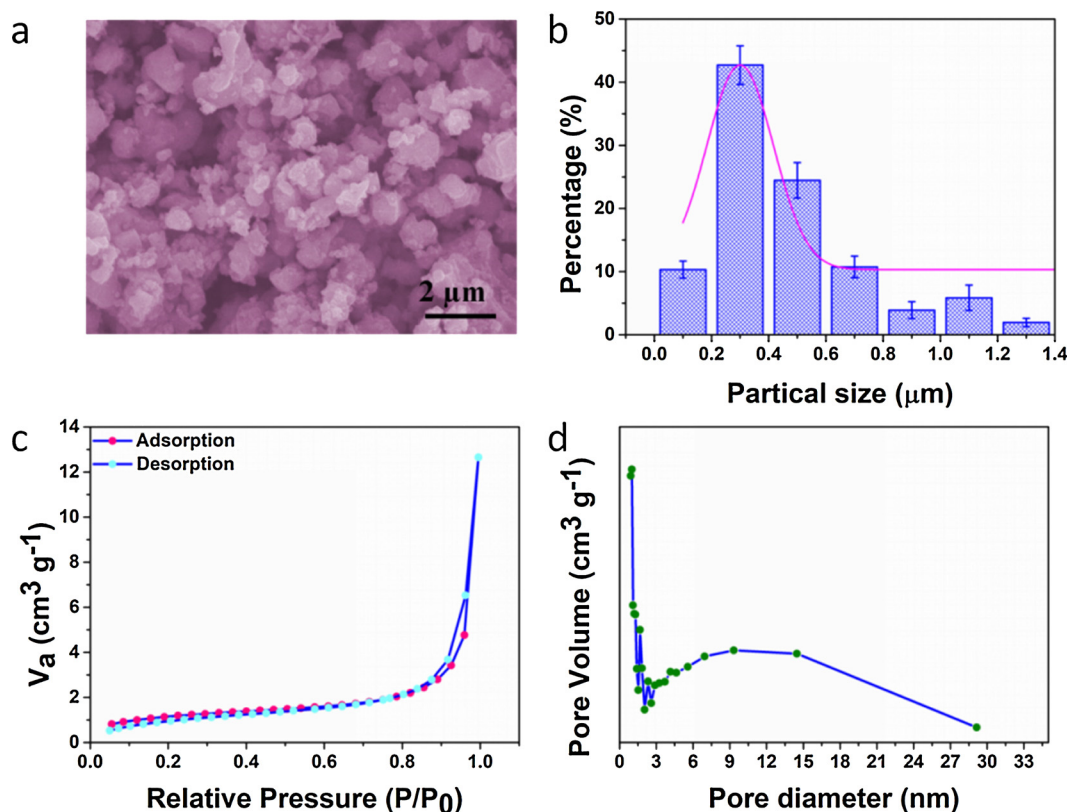

Fig. 3. a) SEM image of β-Fe$_2$O$_3$ at low magnification. b) The particle size distribution of β-Fe$_2$O$_3$ particles. c) Nitrogen adsorption-desorption isotherms. d) Pore size distribution of β-Fe$_2$O$_3$ based on BJH model.
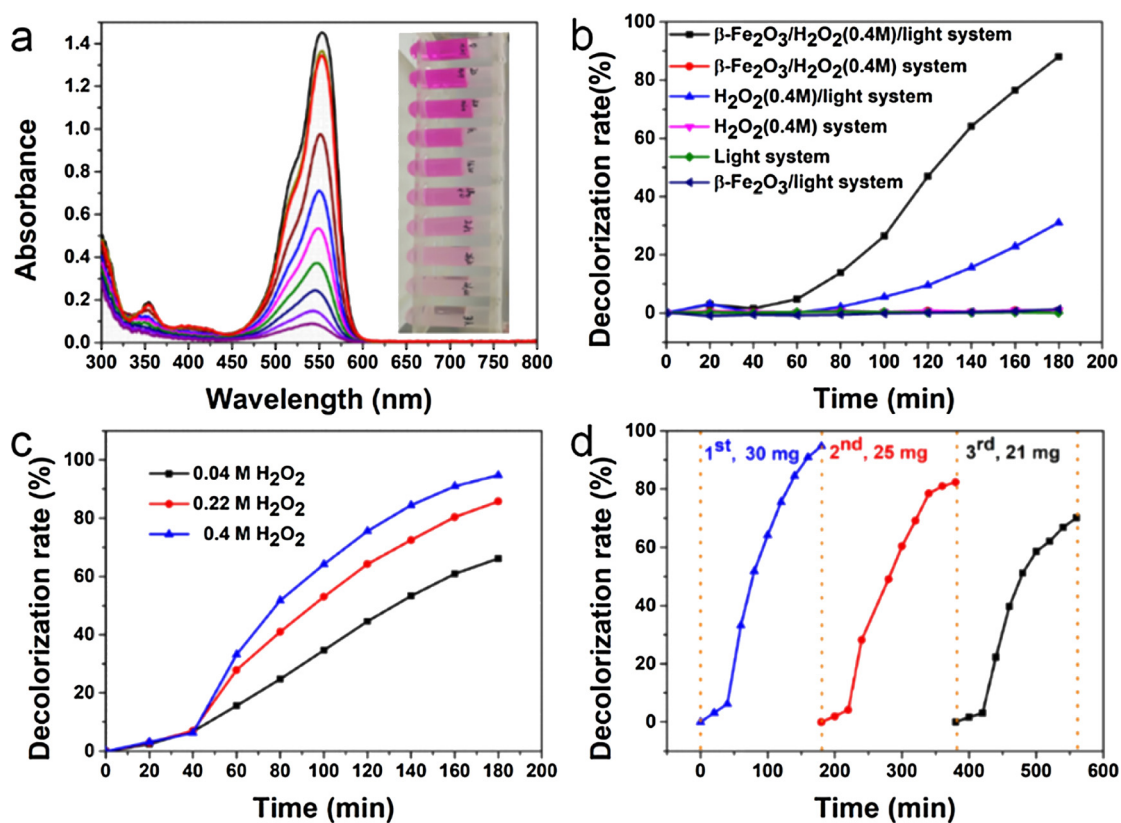
Fig. 4. a) UV–vis spectral changes for RhB degradation with β-Fe$_2$O$_3$/H$_2$O$_2$/light system. b) Time dependent RhB solution degradation under different condition. c) Effect of H$_2$O$_2$ content on the photo-Fenton degradation of RhB. d) Recycled performance of β-Fe$_2$O$_3$/H$_2$O$_2$/Vis system for degradation of RhB dye.

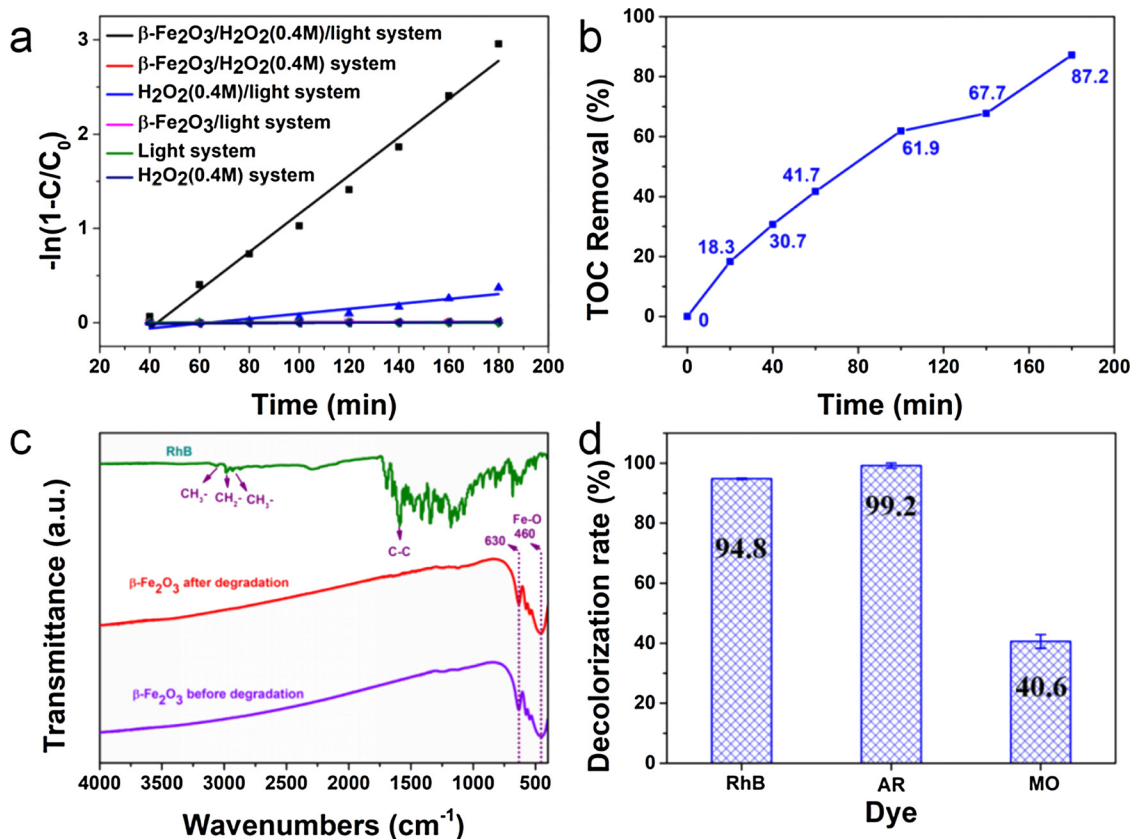**Fig. 5.** a) Comparison of the rate constant (k) for different reaction systems. b) TOC change. c) FT-IR spectra of RhB, β-Fe$_2$O$_3$ before degradation and β-Fe$_2$O$_3$ after degradation. d) Comparison of degradation effect of three kinds of dye.
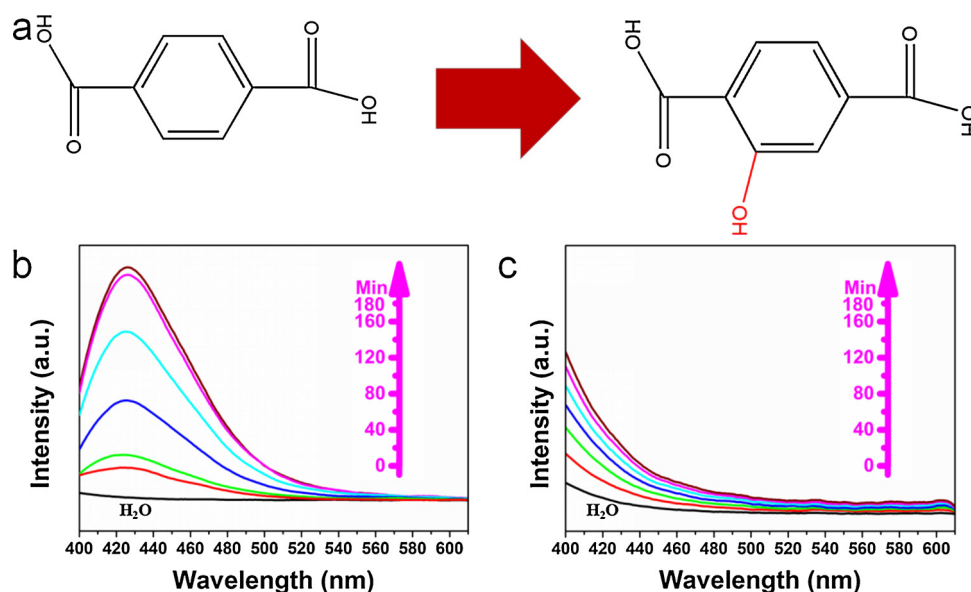
Fig. 6. a) The process of combining TA with ·OH to form TAOH. b) PL spectra of the aqueous solution of terephthalic acid in the β-Fe$_2$O$_3$/H$_2$O$_2$/light system in the time range of. c)PL spectra of the aqueous solution of terephthalic acid in the β-Fe$_2$O$_3$/light system.

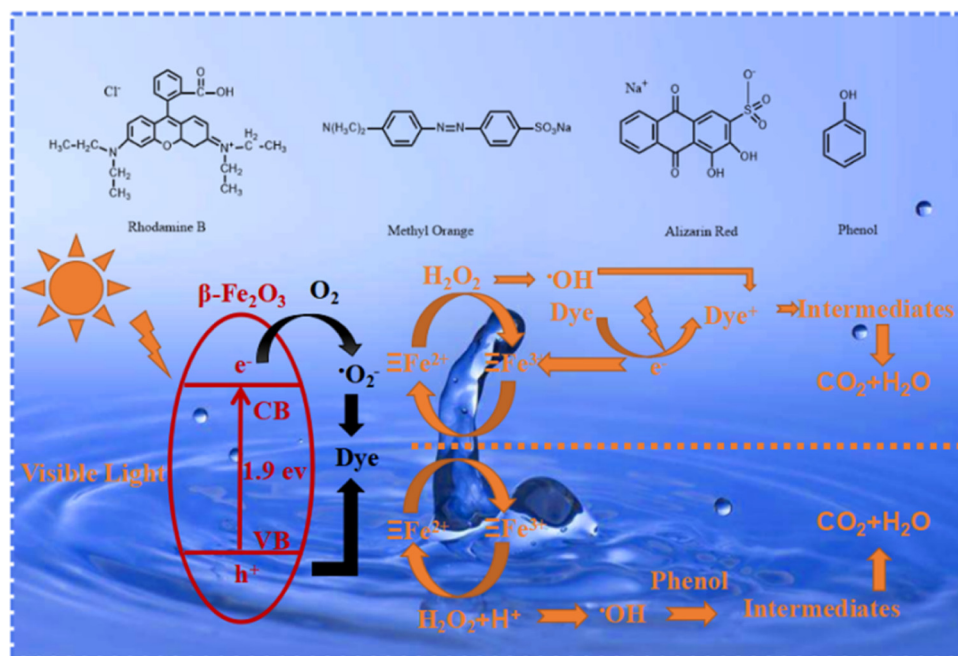**Fig. 7.** Illustration of photo-Fenton reactions mechanisms with β-Fe$_2$O$_3$ (The black indicator lines indicated almost no occurrence in the β-Fe$_2$O$_3$/light system, and the yellow indicator lines indicated that it may happen) (For interpretation of the references to colour in this figure legend, the reader is referred to the web version of this article).

using the BET method. As noted in Fig. 3c, the isotherms were classified as type IV with H$_2$ hysteresis loops (0.5–1 P/P$_0$) according to the IUPAC (International Union of Pure and Applied Chemistry) classification, and the specific surface area of β-Fe$_2$O$_3$ reached 6.4 m^2 g^{-1}. A long and narrow hysteresis loop appeared when the relative pressure was greater than 0.8, which meant that their pore size distributions were not uniform [52], and the mesopores distributions were consistent with the previous analysis (Fig. 3d)

As-prepared β-Fe$_2$O$_3$ without any impurity was used as a catalyst for photo-Fenton reaction for degradation of dyes. Fig. 4 showed RhB degradation via β-Fe$_2$O$_3$/H$_2$O$_2$/light system. A series of characteristic adsorption peaks of RhB solution at 525–550 nm on the UV–vis spectrum were heed. A slight blue shift at the same time as the intensity gradually decreased with increasing irradiation time, and the pink solution also became colorless (inset in Fig. 4a), suggesting that RhB was decomposed by direct cleavage of the conjugated chromophore

structure [47]. To better understand the degradation process, β-Fe$_2$O$_3$/H$_2$O$_2$, H$_2$O$_2$/light, H$_2$O$_2$, light and β-Fe$_2$O$_3$/light systems were also studied as controlled experiment**s,** which excluded the self-photolysis of RhB under visible light irradiation. The concentration of RhB was basically unchanged except for the H$_2$O$_2$/light system, which indicated that the degradation of RhB was caused by highly oxidative hydroxyl radicals. It may result from the fact that the light promoted the production of ·OH on β-Fe$_2$O$_3$ catalysts. We had also repeated experiment (Fig. S5) in order to ensure the accuracy of the results in the β-Fe$_2$O$_3$/H$_2$O$_2$/light system, and the degradation removal rate reached 94.8% within 3 h containing adsorption equilibrium time. At the same time, because the samples exhibited weak magnetic properties, the recycling of the sample was convenient (the inset in Fig. S5). For the stability of β-Fe$_2$O$_3$ (Fig. S6) that continuous illumination did not cause phase change. Simultaneously, the increase of H$_2$O$_2$ dosages could also enhance the decomposition of RhB in β-Fe$_2$O$_3$/H$_2$O$_2$/light system due to
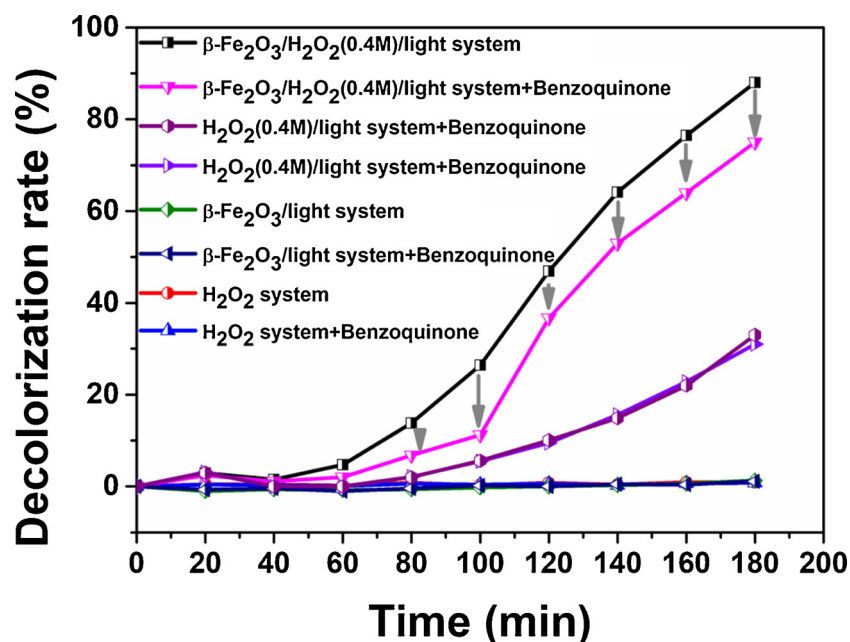
Fig. 8. Time dependent RhB solution degradation under different condition (applying the benzoquinone (0.001 M) to act as the scavenger of ·O_2).

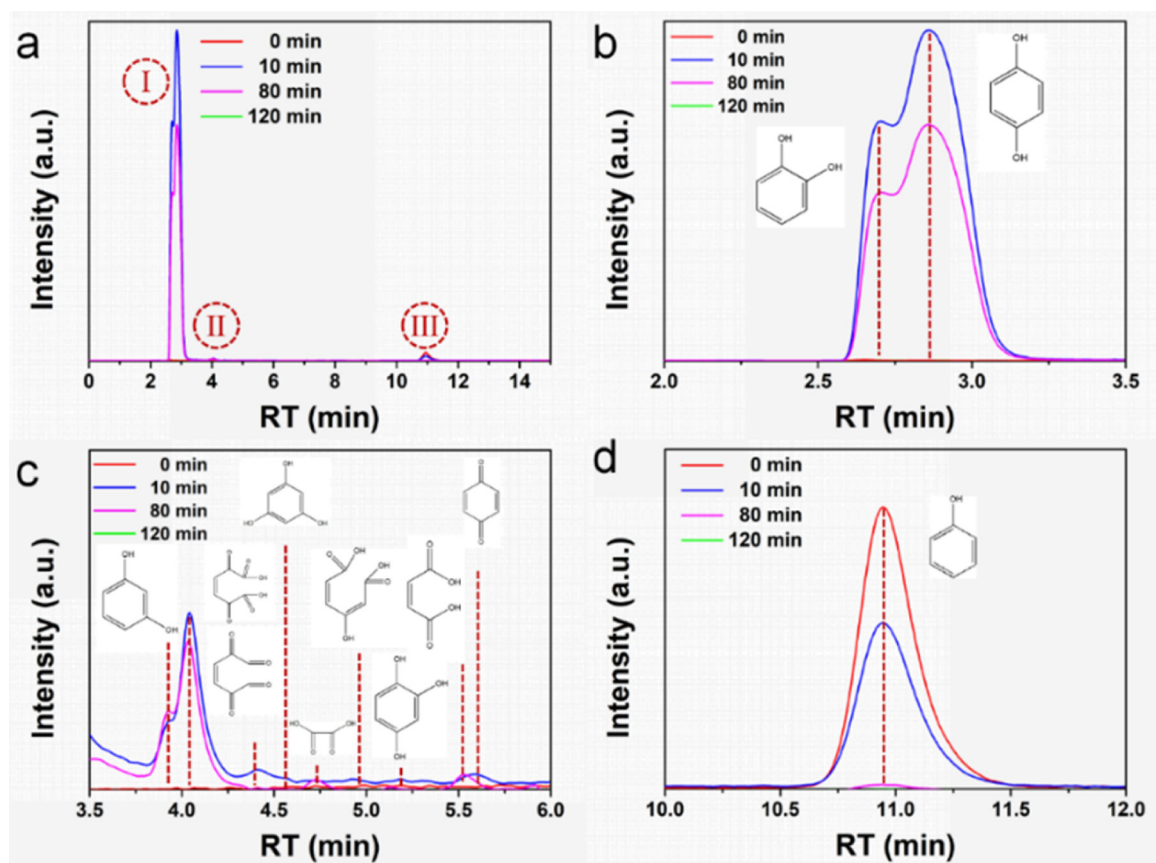**Fig. 9.** a) HPLC diagrams during phenol oxidation in β-Fe_2O_3/H_2O_2/light system (RT: Retention Time). b) LC diagrams for phenol oxidation after 80 min in the β-Fe_2O_3/H_2O_2/light system. b), c) and d) correspond to I, II and III in Fig. 8(a), respectively.

the formation of abundant hydroxyl radicals. (Fig. 4c). Fig. 4d shows that the removal efficiency remained at a level of near 70.2% after three successive cycling runs although the quality of the catalyst was reduced during repeated filtration and washing, which intimated that catalytic activity of β-Fe_2O_3 remained excellent stability.

As shown in Fig. 5a, the apparent kinetic rate constant k can be calculated by the equation of $-\ln(1-C/C_0) = k \times t$ following pseudo first order kinetics for the degradation of RhB. The apparent kinetic rate was 2.027×10^{-2} min^{-1} in the β-Fe_2O_3/H_2O_2/light system, which was higher than the /H_2O_2/light systems, yet the other system exhibited basically no effect. Therefore, we can conclude that the presence of the catalyst promoted the decomposition of hydrogen peroxide to produce
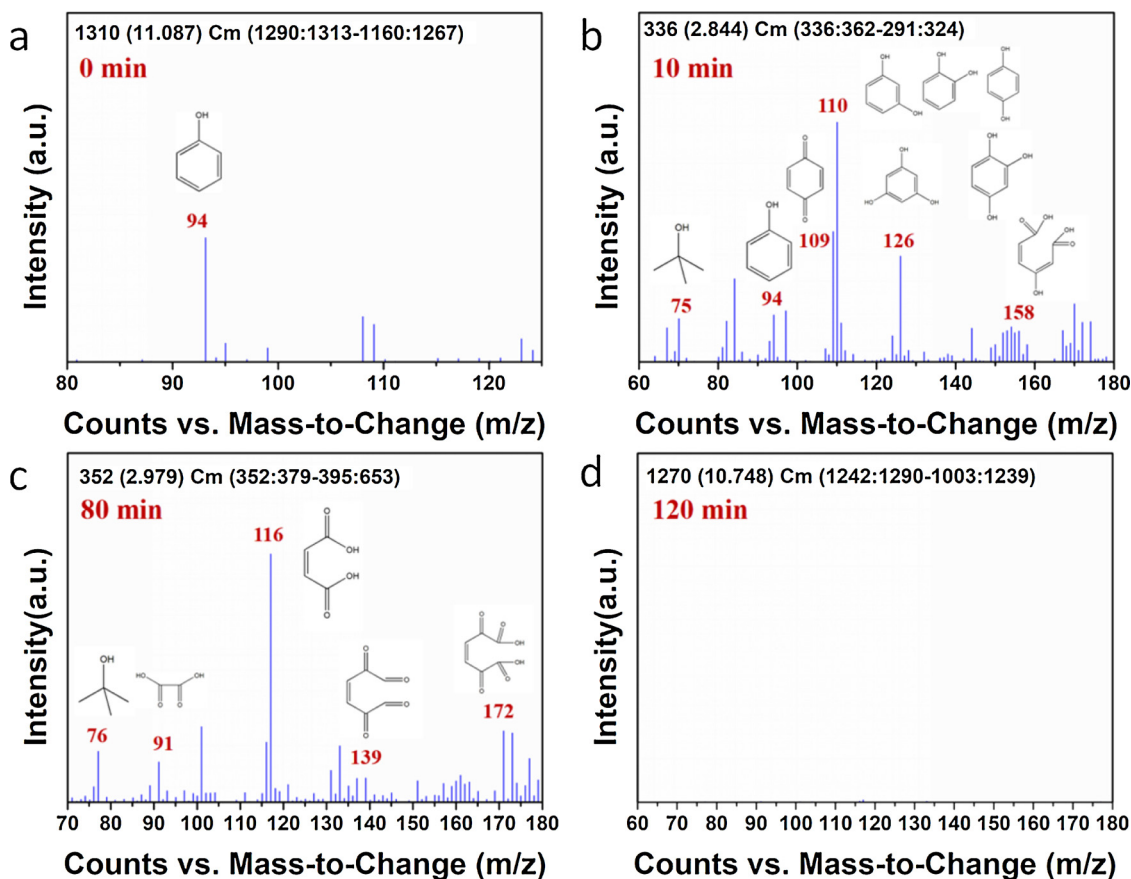
Fig. 10. a) Initial phenol solution mass spectrometry. b) Mass spectrometry after 10 min reaction. c) Mass spectrometry after 80 min reaction. d) Mass spectrometry after 120 min reaction.
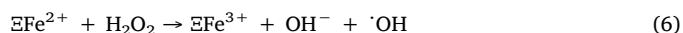
plentiful hydroxyl radicals. The TOC removal value (Fig. 5b) was reached to 87.2% after irradiation. Meanwhile, the result in Fig. 5c was consistent with the above analysis because vibration peaks of dye molecules were not found on β-Fe$_2$O$_3$ before and after degradation. This implied that the β-Fe$_2$O$_3$ did not carry dye molecules after the reaction, which was used to assist in confirming the dominant of chemical degradation process. The other two kinds of dye were also carried out to prove the universality of β-Fe$_2$O$_3$/H$_2$O$_2$/light system (Fig. 5d).

Iron leaching problem must be focused [53,54] in the photo-Fenton reaction. Therefore, the total iron content of the solution (pH ≈ 4.5) after the reaction was determined the AAS (the detection limit was 10^{-3} mg/L). According to the test result, the total iron contents in β-Fe$_2$O$_3$/H$_2$O$_2$/light/RhB and β-Fe$_2$O$_3$/H$_2$O$_2$/light/phenol were lower than the detection limit of the instrument, so it met the legal limit of the European Union as an application prospect.

The degradation of organic contaminants was due to ·OH generated in the photo-Fenton reaction, which was a widely accepted view. As we know, the terephthalic acid (TA) can combine with ·OH to produce 2-hydroxyterephthalic acid (TAOH) (Fig. 6a), which can be used to judge the amount of ·OH by the PL technique. When the excitation wavelength was set at 315 nm according to the literature [24], the maximum fluorescence intensity peak of TAOH appeared at 425 nm. The results in Fig. 6b also corresponded to this statement. The fluorescence intensity gradually increased in β-Fe$_2$O$_3$/H$_2$O$_2$/light system as time increased. Contrary to this, there was no significant change in fluorescence intensity over time in β-Fe$_2$O$_3$/light system (Fig. 6c), implying that there was no ·OH.

Combining with the analysis of the above experimental data, the possible mechanisms for these processes were shown in Fig. 7. Eq. (4) occurred in β-Fe$_2$O$_3$/H$_2$O$_2$/light system, the dye was excited into dye$^+$ under visible light and the resulting electron was transferred to the surface of the β-Fe$_2$O$_3$ to reduce the ΞFe^{3+} into ΞFe^{2+} (Eq. (5)). ΞFe^{2+} will react with H$_2$O$_2$ to produce ·OH for the degradation of organic contaminants and the resulting ΞFe^{3+} will continue to be recycled (Eq. (6)). In addition, H$_2$O$_2$ also produced ·OH under the promotion of light (Eq. (7)), which degraded organic contaminants. We noticed that a large number of ·OH were detected in the β-Fe$_2$O$_3$/H$_2$O$_2$/light system, while β-Fe$_2$O$_3$/light system was the opposite. It can be discovered that the presence of β-Fe$_2$O$_3$ accelerates the decomposition of H$_2$O$_2$ combined with the H$_2$O$_2$/light system and accelerated the degradation rate.

$$Dye + h\nu \rightarrow Dye^+ + e^- \tag{4}$$

$$\Xi Fe^{3+} + e^- \rightarrow \Xi Fe^{2+} \tag{5}$$

$$\Xi Fe^{2+} + H_2O_2 \rightarrow \Xi Fe^{3+} + OH^- + \cdot OH \tag{6}$$

$$H_2O_2 + h\nu \rightarrow OH^- + \cdot OH \tag{7}$$

$$\beta\text{-}Fe_2O_3 + h\nu \rightarrow h^+ + e^- \tag{8}$$

$$O_2 + e^- \rightarrow \cdot O_2 \tag{9}$$

In the photoelectrochemical water splitting, the hydrogen peroxide acted as the hole scavenger, which can reduce photoinduced electron-hole recombination. Hence, the photocurrent density of β-Fe$_2$O$_3$ photoanodes were measured under AM 1.5 G sunlight illumination (100 mW cm^{-2}) and 300 W Xenon lamp in Fig. S7. It can be clearly observed that when a small amount of H$_2$O$_2$ was added, the photocurrent increased obviously.

There were some opinions that superoxide radicals (·O$_2$) can also participate in the degradation of organic contaminants as active species in the photocatalyst/light system [40]. Hydrogen peroxide may act as a hole sacrificial agent to increase the electron concentration on the surface of the photocatalyst, thus triggering the photocatalyst/light
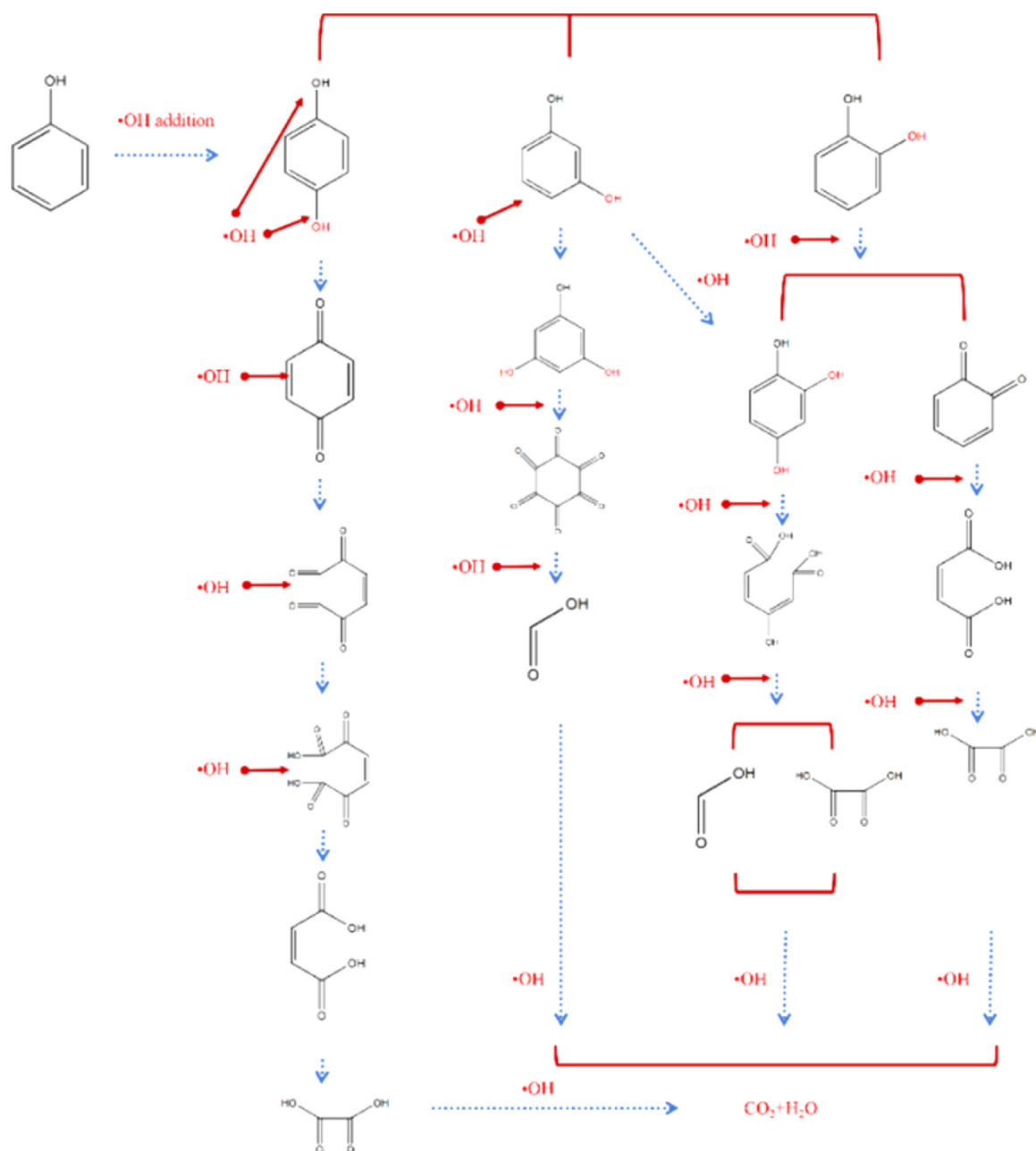
Fig. 11. Mechanism of phenol oxidation in the β-Fe$_2$O$_3$/H$_2$O$_2$/light system.

system to produce a small amount of ˙O$_2$ in the photocatalyst/H$_2$O$_2$/ light system. Applying benzoquinone often as the scavenger of ˙O$_2$, we designed a series of experiments to explore the possibility of ˙O$_2$. Intuitively, extending the irradiation time did not increase the effect of degradation (Fig. S8) in the β-Fe$_2$O$_3$/light system, so we inferred that the system did not react according to Eqs. (8 and 9). In other words, there was no active species (˙O$_2$ and ˙OH). But in the β-Fe$_2$O$_3$/H$_2$O$_2$/ light system, on the basis of the existence of a large number of hydroxyl radicals, it was obvious that the removal rate of degradation will decrease in Fig. 8 (the gray pointed part represented the reduction of a small amount of ˙O$_2$) when the benzoquinone was added. Therefore, the reactions in the Eqs. (8and9) were very likely to happen in β-Fe$_2$O$_3$/ H$_2$O$_2$/light.

Although the chromogenic reaction (Fig. S9) can be used to detect the change in concentration for phenol, it did not reflect the intermediates and whether they were completely degraded. We analyzed the pathway of phenol oxidation by LC−MS. In Fig. 9a, the signal intensity

of phenol gradually decreased with time, while the signal peaks of the intermediates appeared and then weakened until they disappeared. According to the standard compounds, the intermediates of phenol oxidation were identified. Partial amplification (Fig. 9b) from part I of Fig. 9a shows the peak of catechol (RT:2.702) and hydroquinone (RT:2.86). More chromatographic peaks of intermediates were identified within 3.5 to 6 min of retention time in Fig. 9c, for example, resorcinol (RT:3.918), carboxylic acids (RT:4.043), aldehydes (RT:4.41), phloroglucinol (RT:4.568), oxalic acid (RT:4.727), carboxylic acids with hydroxyl group (RT:4.935), 1,2,4-benzenetriol (RT:5.193), maleic acid (RT:5.527) and p-Quinone (RT:5.593). Simultaneously, Fig. 9d clearly shows the peak of phenol (RT:10.952). Moreover, the mass spectrum (Fig. 10) reflected the molecular weight of the intermediates in the solution, which was valuable for analyzing the oxidation process. When the unreacted solution was mostly phenol, a small part of the decomposition will occur due to its own instability (Fig. 10a). After 10 min, the typical hydroquinone, catechol, resorcinol and so on can be
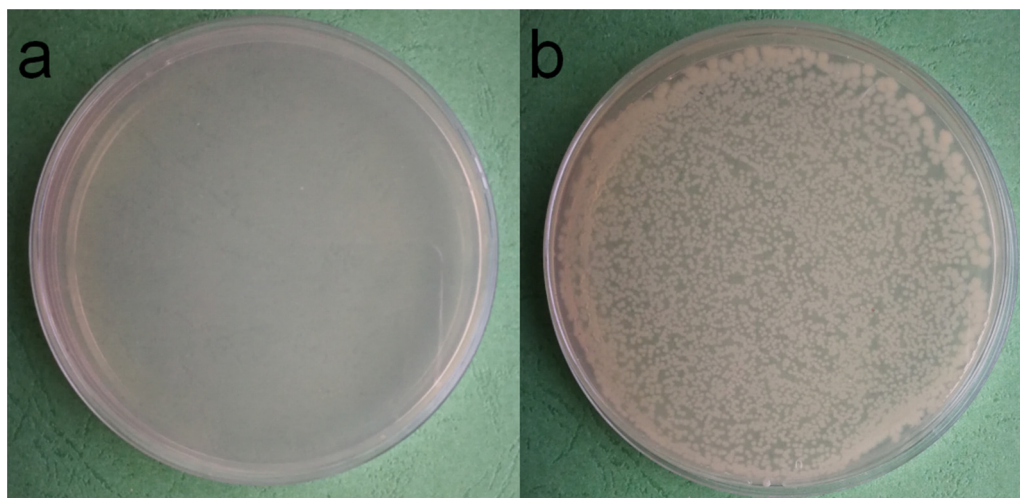
Fig. 12. Photograph of antibacterial activity of phenol solutions before (a) and after (b) degradation in the β-Fe$_2$O$_3$/H$_2$O$_2$/light system.

clearly observed in Fig. 10b. As the reaction time progresses, some smaller molecular weight intermediates were identified after 80 min (Fig. 10c). Finally, the corresponding intermediates were not detected in 120 min (Fig. 10d). Unexpectedly, this result fitted well with the color reaction.

As shown in the Fig. 11, the specific mechanism of phenol oxidation was deduced in the β-Fe$_2$O$_3$/H$_2$O$_2$/light system due to the intermediates which were detected. The detailed process was as follows. When phenol was attacked by the ·OH, the most probable intermediates were formed, including hydroquinone, catechol and resorcinol. Hydroquinone first formed p-Quinone under the action of ·OH, and ·OH react with carbon-carbon double bonds to form aldehydes, which were subsequently oxidized to carboxylic acids [55]. On one hand, resorcinol formed phloroglucinol under the action of ·OH, which were oxidized to be cyclohexanone, and further oxidized to a small molecule carboxylic acid. On the other hand, it may be similar to hydroquinone for the oxidation process of catechol. The other may be the first to form 1,2,4-benzenetriol (It may also be formed from resorcinol), which was further oxidized to carboxylic acids by the hydroxyl radical groups with ring opening reaction [56]. The acetic acid and formic acid decomposed from the above were finally mineralized into CO$_2$ and H$_2$O.

For the sake of potential application in the β-Fe$_2$O$_3$/H$_2$O$_2$/light system, the toxicity of the phenol solution before and after the reaction was reflected by the growth state of the *Escherichia coli* (*E. coli*) according to the previous related report [57]. In particular, the nutrient broth, diluents and glassware used in the experiment were sterilized at high temperatures. In detail, cultivating the bacterial cells with 60 ml of nutrient broth were at 37 °C for 20 h, then the colony concentration was about 10^7 cfu (colony forming units)/mL obtained by the plate counting method. Further, the above colonies were diluted 500 times. Subsequently, 100 μl of the above solution was taken out and combined thoroughly with 2 ml of the solution before and after degradation filtered through a sterile filter. Ultimately, 50 μl of the amalgamated solution was incubated on agar plate at 37 °C for 24 h. As can be seen from Fig. 12, the number of *E. coli* bacterial colonies in the solution after degradation was significantly increased, revealing that the antibacterial activity of the solution was reduced, thus reflecting the elimination of toxicity of the phenol solution. However, due to the strong bactericidal action of hydrogen peroxide, in order to avoid the influence of the toxicity judgment of phenol solution, so we selected the other three solutions (0.4 M H$_2$O$_2$, 3 mg/L phenol, 300 mg/L phenol) to compare in Fig. S10. It can be concluded that the toxicity of low concentration phenol solution was not enough to completely inactivate *E. coli* bacterial colonies, and the significantly increased toxicity of high concentration made the number of *E. coli* bacterial colonies very low.

4. Conclusion

In conclusion, β-Fe$_2$O$_3$ was found to be a low-cost, non-toxic, and efficient catalyst for photo-Fenton reaction, which was as a direct bandgap semiconductor with wide spectral response. Especially for the degradation of phenol, we applied LC−MS to explore possible degradation pathways. The major intermediates produced by hydroxylation of phenol were detected, which were converted into H$_2$O and CO$_2$ eventually. As one of the advanced oxidation technologies, it suggested that the β-Fe$_2$O$_3$/H$_2$O$_2$/light system will be potentially applied to actual production more and more well.

Appendix A. Supplementary data

Supplementary material related to this article can be found, in the online version, at doi:https://doi.org/10.1016/j.apcatb.2019.01.003.

References

[1] K. Kümmerer, The presence of pharmaceuticals in the environment due to human use- present knowledge and future challenges, J. Environ. Manage. 90 (2009) 2354–2366.
[2] H.X. Qi, Y.Y. Zhuang, Y.C. Yuan, W.X. Gu, Decomposition of aniline in supercritical water, J. Hazard. Mater. 90 (2002) 51–62.
[3] W.H. Glaze, J. Kangt, Advanced oxidation processes. Test of a kinetic model for the oxidation of organic compounds with ozone and hydrogen peroxide in a semibatch reactor, Ind. Eng. Chem. Res. 28 (1989) 1580–1587.
[4] J.M. Clomburg, A.M. Crumbley, R. Gonzalez, Industrial biomanufacturing: the future of chemical production, Science 355 (2017) 0804.
[5] S.M. Mintenig, I.I. Veen, M.G. Löder, S. Primpke, G. Gerdts, Identification of microplastic in effluents of waste water treatment plants using focal plane array-based micro-Fourier-transform infrared imaging, Water Res. 108 (2017) 365–372.
[6] Y. Yang, J.J. Pignatello, J. Ma, W.A. Mitch, Comparison of halide impacts on the efficiency of contaminant degradation by sulfate and hydroxyl radical-based advanced oxidation processes (AOPs), Environ. Sci. Technol. 48 (2014) 2344–2351.
[7] S.N. Guo, Y. Zhu, Y.Y. Yan, Y.L. Min, J.C. Fan, Q.J. Xu, Holey structured graphitic carbon nitride thin sheets with edge oxygen doping via photo-Fenton reaction with enhanced photocatalytic activity, Appl. Catal. B 185 (2016) 315–321.
[8] M. Xing, W. Xu, C. Dong, Y.C. Bai, J.B. Zeng, Y. Zhou, J.L. Zhang, Y.D. Yin, Metal sulfides as excellent Co-catalysts for H$_2$O$_2$ decomposition in advanced oxidation processes, Chem 4 (2018) 1359–1372.
[9] C. Zhang, Y. Ou, W.X. Lei, L.S. Wan, J.Ji, Z.K. Xu. CuSO$_4$/H$_2$O$_2$-Induced Rapid

Deposition of Polydopamine Coatings with High Uniformity and Enhanced Stability, Angew. Chem. Int. Ed 55 (2016) 3054–3057.

[10] P. Drzewicz, L. Perez-Estrada, A. Alpatova, J.W. Martin, M.G. El-Din, Impact of peroxydisulfate in the presence of zero valent iron on the oxidation of cyclohexanoic acid and naphthenic acids from oil sands process-affected water, Environ. Sci. Technol. 46 (2012) 8984–8991.

[11] L. Varanasi, E. Coscarelli, M. Khaksari, L.R. Mazzoleni, D. Minakata, Transformations of dissolved organic matter induced by UV photolysis, Hydroxyl radicals, chlorine radicals, and sulfate radicals in aqueous-phase UV-Based advanced oxidation processes, Water Res. 135 (2018) 22–30.

[12] Y.Y. Xiang, J.Y. Fang, C. Shang, Kinetics and pathways of ibuprofen degradation by the UV/chlorine advanced oxidation process, Water Res. 90 (2016) 301–308.

[13] Y.Q. Liu, X.X. He, Y.S. Fu, D.D. Dionysiou, Degradation kinetics and mechanism of oxytetracycline by hydroxyl radical-based advanced oxidation processes, Chem. Eng. J. 284 (2016) 1317–1327.

[14] F.C. Moreira, R.A.R. Boaventura, E. Brillas, V.J.P. Vilar, Electrochemical advanced oxidation processes: a review on their application to synthetic and real wastewaters, Appl. Catal. B 202 (2017) 217–261.

[15] Y.Y. Liu, W. Jin, Y.P. Zhao, G.S. Zhang, W. Zhang, Enhanced catalytic degradation of methylene blue by α-Fe$_2$O$_3$/graphene oxide via heterogeneous photo-Fenton reactions, Appl. Catal. B 206 (2017) 642–652.

[16] N.F.F. Moreira, C. Narciso-da-Rocha, M. Inmaculada Polo-López, L.M. Pastrana-Martinez, J.L. Faria, C.M. Manaia, P. Fernandez-Ibanez, O.C. Nunes, A.M.T. Silva, Solar treatment (H$_2$O$_2$, TiO$_2$-P25 and GO-TiO$_2$ photocatalysis, photo-Fenton) of organic micropollutants, human pathogen indicators, antibiotic resistant bacteria and related genes in urban wastewater, Water Res. 135 (2018) 195–206.

[17] L. Clarizia, D. Russo, I. Di Somma, R. Marotta, R. Andreozzi, Homogeneous photo-Fenton processes at near neutral pH: a review, Appl. Catal. B 209 (2017) 358–371.

[18] F. Martínez, G. Calleja, J.A. Melero, R. Molina, Iron species incorporated over different silica supports for the heterogeneous photo-Fenton oxidation of phenol, Appl. Catal. B 70 (2007) 452–460.

[19] D.A.C. Coledam, I. Sánchez-Montes, B.F. Silva, J.M. Aquino, On the performance of HOCl/Fe^{2+}, HOCl/Fe^{2+}/UVA, and HOCl/UVC processes using in situ, electro-generated active chlorine to mineralize the herbicide picloram, Appl. Catal. B 227 (2018) 170–177.

[20] J. Porras, S. Giannakis, R.A. Torres-Palma, J.J. Fernandez, M. Bensimon, C. Pulgarin, Fe and Cu in humic acid extracts modify bacterial inactivation pathways during solar disinfection and photo-Fenton processes in water, Appl. Catal. B 235 (2018) 75–83.

[21] T. Soltani, B.K. Lee, Enhanced formation of sulfate radicals by metal-doped BiFeO$_3$ under visible light for improving photo-Fenton catalytic degradation of 2-chlorophenol, Chem. Eng. J. 313 (2017) 1258–1268.

[22] T. Soltani, B.K. Lee, Novel and facile synthesis of Ba-doped BiFeO$_3$ nanoparticles and enhancement of their magnetic and photocatalytic activities for complete degradation of benzene in aqueous solution, J. Hazard. Mater. 316 (2016) 122–133.

[23] H.T. Dang, T.M.T. Nguyen, T.T. Nguyen, S.Q. Thi, H.T. Tran, H.Q. Tran, T.K. Le, Magnetic CoFe$_2$O$_4$Prepared by Polymeric Precursor Method as a Reusable Heterogeneous Fenton-Like Catalyst for the Efficient Removal of Methylene Blue, Chem. Eng. Commun. 203 (2016) 1260–1268.

[24] H.B. Chen, W.X. Liu, Z.Z. Qin, ZnO/ZnFe$_2$O$_4$ nanocomposite as a broad-spectrum photo-Fenton-like photocatalyst with near-infrared activity, Catal. Sci. Technol. 7 (2017) 2236–2244.

[25] X.J. Guo, K.B. Wang, D. Li, J.B. Qin, Heterogeneous photo-Fenton processes using graphite carbon coating hollow CuFe$_2$O$_4$ spheres for the degradation of methylene blue, Appl. Surf. Sci. 420 (2017) 792–801.

[26] H. Tian, J. Peng, Q. Du, X.H. Hui, H. He, One-pot sustainable synthesis of magnetic MIL-100 (Fe) with novel Fe$_3$O$_4$ morphology and its application in heterogeneous degradation, Dalton Trans. 47 (2018) 3417–3424.

[27] H.C. Lan, A.M. Wang, R.P. Liu, H.J. Liu, J.H. Qu, Heterogeneous photo-Fenton degradation of acid red B over Fe$_2$O$_3$ supported on activated carbon fiber, J. Hazard. Mater. 285 (2015) 167–172.

[28] X.J. Yang, Y.W. Sun, H.M. Sun, L.S. Zhang, L.J. Zhao, J.S. Lian, Q. Jiang, High efficient photo-fenton catalyst of α-Fe$_2$O$_3$/MoS$_2$ hierarchical nano heterostructures: reutilization for supercapacitors, Sci. Rep. 6 (2016) 31591.

[29] X. Wang, J.Q. Wang, Z.T. Cui, S.G. Wang, M.H. Cao, Facet effect of a-Fe$_2$O$_3$ crystals on photocatalytic performance in the photo-Fenton reaction, RSC Adv. 4 (2014) 34387–34394.

[30] C. Xiao, J. Li, G.K. Zhang, Synthesis of stable burger-like α-Fe$_2$O$_3$ catalysts: formation mechanism and excellent photo-Fenton catalytic performance, J. Clean. Prod. 180 (2018) 550–559.

[31] X.F. Qian, Y.W. Wu, M. Kan, M.Y. Fang, D.T. Yue, J. Zeng, Y.X. Zhao, FeOOH quantum dots coupled g-C$_3$N$_4$ for visible light driving photo- Fenton degradation of organic pollutants, Appl. Catal. B 237 (2018) 513–520.

[32] L.Q. Guo, F. Chen, X.Q. Fan, W.D. Cai, J.L. Zhang, S-doped-Fe$_2$O$_3$ as a highly active heterogeneous Fenton-like catalyst towards the degradation of acid orange 7 and phenol, Appl. Catal. B 96 (2010) 162–168.

[33] H. Chen, Z.L. Zhang, Z.L. Yang, Q. Yang, B. Li, Z.Y. Bai, Heterogeneous Fenton-like catalytic degradation of 2, 4-dichlorophenoxyacetic acid in water with FeS, Chem. Eng. J. 273 (2015) 481–489.

[34] Y.L. Zhang, K. Zhang, C.M. Dai, X.F. Zhou, H.P. Si, An enhanced Fenton reaction catalyzed by natural heterogeneous pyrite for nitrobenzene degradation in an aqueous solution, Chem. Eng. J. 244 (2014) 438–445.

[35] X. Huang, Y. Niu, W. Hu, Fe/Fe$_3$C nanoparticles loaded on Fe/N-doped graphene as an efficient heterogeneous Fenton catalyst for degradation of organic pollutants, Colloids Surf. A Physicochem. Eng. Asp. 518 (2017) 145–150.

[36] W. Shi, D. Du, B. Shen, C.F. Cui, L.J. Lu, L.Z. Wang, J.L. Zhang, Synthesis of yolk−Shell structured Fe$_3$O$_4$@void@CdS nanoparticles: a general and effective structure design for photo-fenton reaction, ACS Appl. Mater. Interfaces 8 (2016) 20831–20838.

[37] Y.Y. Liu, W. Jin, Y.P. Zhao, G.S. Zhang, W. Zhang, Enhanced catalytic degradation of methylene blue by α-Fe$_2$O$_3$/graphene oxide via heterogeneous photo-Fenton reactions, Appl. Catal. B 206 (2017) 642–652.

[38] C.K. Christoforidis, T. Montini, E. Bontempi, S. Zafeiratos, J.J.D. Jaén, P. Fornasiero, Synthesis and photocatalytic application of visible-light active β-Fe$_2$O$_3$/g-C$_3$N$_4$ hybrid nanocomposites, Appl. Catal. B 187 (2016) 171–180.

[39] D. Du, W. Shi, L.Z. Wang, J.L. Zhang, Yolk-shell structured Fe$_3$O$_4$@void@TiO$_2$ as a photo-Fenton-like catalyst for the extremely efficient elimination of tetracycline, Appl. Catal. B 200 (2017) 484–492.

[40] S.Q. Huang, Y.G. Xu, T. Zhou, M. Xie, Y. Ma, Q.Q. Liu, L.Q. Jing, H. Xu, H.M. Li, Constructing magnetic catalysts with in-suit solid-liquid interfacial photo-Fenton-like reaction over Ag$_3$PO$_4$@NiFe$_2$O$_4$ composites, Appl. Catal. B 225 (2017) 40–50.

[41] Y.H. Zhang, Y. Su, Y.Q. Wang, J.B. He, G.L. McPherson, V.T. John, Rapid fabrication of hollow and yolk-shell α-Fe$_2$O$_3$ particles with applications to enhanced photo-Fenton reactions, RSC Adv. 62 (2017) 39049–39056.

[42] D. Bin Jiang, X.Y. Liu, X. Xu, Y.X. Zhang, Double-shell Fe$_2$O$_3$ hollow box-like structure for enhanced Photo-Fenton degradation of Malachite green dye, J. Phys. Chem. Solids 112 (2017) 209–215.

[43] S.N. Xuan, G. Zhang, X. Yang, Mesocrystalline Zn-Doped Fe$_3$O$_4$ hollow submicrospheres: formation mechanism and enhanced photo-fenton catalytic performance, ACS Appl. Mater. Interfaces 9 (2017) 8900–8909.

[44] T. Soltani, B.K. Lee, Improving heterogeneous photo-Fenton catalytic degradation of toluene under visible light irradiation through Ba-doping in BiFeO$_3$ nanoparticles, J. Mol. Catal. A Chem. 425 (2016) 199–207.

[45] J.G. Xu, Y.Q. Li, B.L. Yuan, C.H. Shen, M.L. Fu, H.J. Cui, W.J. Sun, Large scale preparation of Cu-doped α-FeOOH nanoflowers and their photo-Fenton-like catalytic degradation of diclofenac sodium, Chem. Eng. J. 291 (2016) 174–183.

[46] Y.X. Deng, M.Y. Xing, J.L. Zhang, An advanced TiO$_2$/Fe$_2$TiO$_5$/Fe$_2$O$_3$ triple-heterojunction with enhanced and stable visible-light-driven Fenton reaction for the removal of organic pollutants, Appl. Catal. B 211 (2017) 157–166.

[47] N. Wang, Y.C. Du, W.J. Ma, P. Xu, X.J. Han, Rational design and synthesis of SnO$_2$-encapsulated Fe$_2$O$_3$ nanocubes as a robust and stable photo-Fenton catalyst, Appl. Catal. B 210 (2017) 23–33.

[48] Y. Ma, Q. Wang, S.T. Xing, Insight into the catalytic mechanism of γ-Fe$_2$O$_3$/ZnFe$_2$O$_4$ for hydrogen peroxide activation under visible light, J. Colloid Interface Sci. 529 (2018) 247–254.

[49] S. Sakurai, A. Namai, K. Hashimoto, S. Ohkoshi, First observation of phase transformation of all four Fe$_2$O$_3$ phases ($\gamma\rightarrow\epsilon\rightarrow\beta\rightarrow\alpha$), J. Am. Chem. Soc. 131 (2009) 18299–18303.

[50] N.S. Zhang, Y.S. Guo, X. Wang, S.Y. Zhang, Z.S. Li, Z.G. Zou, A beta-Fe$_2$O$_3$ nanoparticle-assembled film for photoelectrochemical water splitting, Dalton Trans. 46 (2017) 10673–10677.

[51] T. Danno, H. Asaoka, M. Nakanishi, T. Fujii, Y. Ikeda, Y. Kusano, J. Takada, Formation mechanism of nano-crystalline β-Fe$_2$O$_3$ particles with bixbyite structure and their magnetic properties, J. Phys. Conf. Ser. 200 (2010) 318–321.

[52] K.S. Walton, R.Q. Snurr, Applicability of the BET method for determining surface areas of microporous metal-organic frameworks, J. Am. Chem. Soc. 129 (2007) 8552–8556.

[53] S. Hartmann, H. Kullmanna, Keller, Wastewater treatment with heterogeneous Fenton-type catalysts based on porous materials, J. Mater. Chem. 20 (2010) 9002–9017.

[54] X.F. Qian, M. Ren, Y. Zhu, D.T. Yue, Y. Han, J.P. Jia, Y.X. Zhao, Visible light assisted heterogeneous fenton-like degradation of organic pollutant via α-FeOOH/Mesoporous carbon composites, Environ. Sci. Technol. 51 (2017) 3993–4000.

[55] Y. Wang, H.L. Tian, Y.G. Yu, C.Z. Hu, Enhanced catalytic activity of α-FeOOH-rGO supported on active carbon fiber (ACF) for degradation of phenol and quinolone in the solar-Fenton system, Chemosphere 208 (2018) 931–941.

[56] M. Diak, M. Klein, T. Klimczuk, W. Lisowski, H. Remita, A.Z. Medynska, E. Grabowska, Photoactivity of decahedral TiO$_2$ loaded with bimetallic nanoparticles: degradation pathway of phenol-1-^{13}C and hydroxyl radical formation, Appl. Catal. B 200 (2017) 56–71.

[57] Y.G. Xu, J. Liu, M. Xie, L.Q. Jing, H. Xu, X.J. She, H.M. Li, J.M. Xie, Construction of novel CNT/LaVO$_4$ nanostructures for efficient antibiotic photodegradation, Chem. Eng. J. 357 (2019) 487–497.